Chapter 4
Introduction of Space Weather Research on Magnetosphere and Ionosphere of the Earth

Kazuo Shiokawa

4.1 Structures of and Variations in Magnetosphere and Ionosphere of the Earth

As shown schematically in Fig 4.1, various space weather events occur in the Earth's magnetosphere and ionosphere, due to emissions and plasma flow from the sun and due to atmospheric waves from the lower atmosphere. Figure 4.2 schematically shows the north-south cross-section of the magnetosphere of the Earth from the side (equatorial direction) and the positions of major satellites in the magnetosphere. The magnetosphere extends to approximately ten times the radius of the Earth (Re) in the solar direction (left side of the figure) (10 Re = ~60,000 km) and has a long tail in the antisolar direction up to several hundred Re. On average, the plasma density in the solar wind is approximately $1–10$ cm^{-3}, whereas it is 0.1 cm^{-3} or less in the magnetosphere close to the solar wind. Thus, the magnetosphere has a low-density bubble-like structure protected by the magnetic field of the Earth within a sea of dense plasma (solar wind) emitted by the Sun. As the magnetosphere reaches a few Re, the plasma density is increased by the outflows from the ionosphere.

Figure 4.2 shows that on the dayside (left side in the figure), a bow shock caused by the high-speed solar wind hitting the magnetosphere is present in front of the magnetosphere. On the downstream side of this bow shock, there is a magnetosheath, in which the magnetic field is highly disturbed. A magnetotail consists of a plasma sheet filled with plasma with energy of several kiloelectron volts (keV), sandwiched between a lobe with a low-density plasma and the strong magnetic field. There is a noticeable boundary between the plasma sheet and the lobe (plasma sheet boundary layer). The plasma sheet extends not only to the nightside (right side in Fig. 4.2) but also to the dayside. The energy of the plasma particles in

K. Shiokawa (✉)

Institute for Space-Earth Environmental Research, Nagoya University, Nagoya, Aichi, Japan
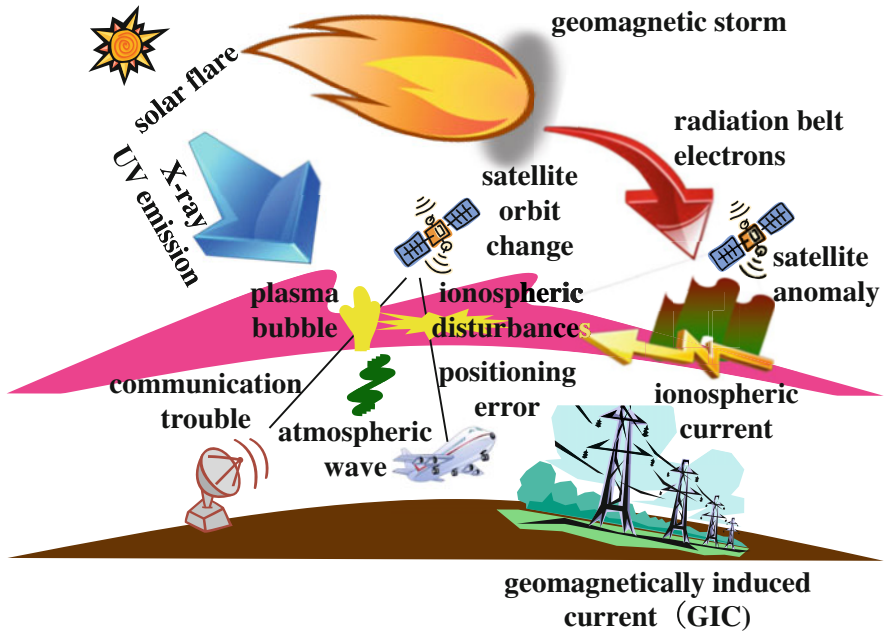e-mail: shiokawa@nagoya-u.jp

Fig. 4.1 Schematic of typical space weather phenomena occurring in magnetosphere and ionosphere of the Earth

the plasma sheet increases as they approach the Earth, forming a ring current region having energy of several tens of keV and radiation belts of several hundred keV to several tens of megaelectron volts (MeV). The distribution of the radiation belt electrons is divided into inner and outer belts by a slot region where the density is low at approximately 2–3 Re. In contrast, a cold and dense ($>10^3$ cm^{-3}) plasma with energy of a few electron volts (eV) flows out from the ionosphere of the Earth, spreading out to ~4 Re and forming a plasmasphere. The outer boundary of the plasmasphere (plasmapause) is frequently a well-defined density boundary. This is because the orbit of the plasma flowing out from the ionosphere is divided into an inner part, which orbits with the rotation of the Earth, and an outer part, which flows away toward the magnetopause by convection (Nishida 1966).

The above magnetospheric structures are mainly characterized by the magnetic field and plasma of the magnetosphere, which are invisible to the naked eye. However, they can be illustrated as in Fig. 4.2 because many satellites have observed the magnetosphere over a long period and statistically investigated the characteristics of its magnetic field and plasma. The solar wind in front of the magnetosphere has a Lagrangian point (L1) where satellites can remain because the gravity of the Sun and the Earth are balanced. The solar wind and the interplanetary magnetic field (IMF), which determines the disturbance levels of the magnetosphere and
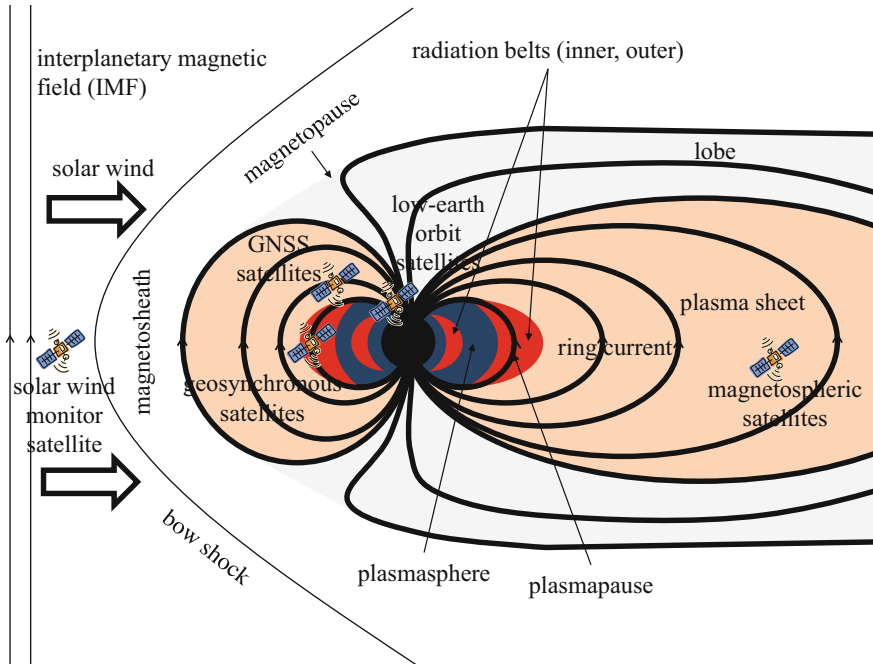
Fig. 4.2 Schematic of north–south cross section of magnetosphere of the Earth viewed from the side (equatorial direction) and locations of major satellites in it

ionosphere of the Earth, can be constantly monitored at L1 point, and they are the main information for space weather forecasting. Geostationary satellites and the Global Navigation Satellite System (GNSS) satellites, which are frequently used for space applications, are located at altitudes of 20,000–40,000 km and are strongly affected by the high-energy plasma in the outer radiation belt. Low-earth orbit (LEO) satellites, such as the International Space Station and Earth observation satellites that image the ground, are also strongly affected by the radiation belts when they pass through orbits near the North and South Poles.

The plasma in the magnetosphere of the Earth is nonstationary; it changes with time with the variations of the solar wind and the IMF. In particular, when the IMF is southward, as shown in Fig. 4.3, the IMF and the magnetic field of the Earth form a magnetic reconnection at the daytime magnetopause, which facilitates the penetration of the magnetic field energy and plasma particles into the magnetosphere (Dungey, 1962). Simultaneously, these reconnected magnetic field lines are swept into the magnetotail and accumulate there, which begins to be compressed from both north and south. This pressure causes the magnetic fields in the Northern and Southern Hemispheres to reconnect in the plasma sheet of the magnetotail. This magnetic reconnection in the magnetotail causes the plasma to be launched in the earthward and counter-earthward directions by the magnetic tension force. The
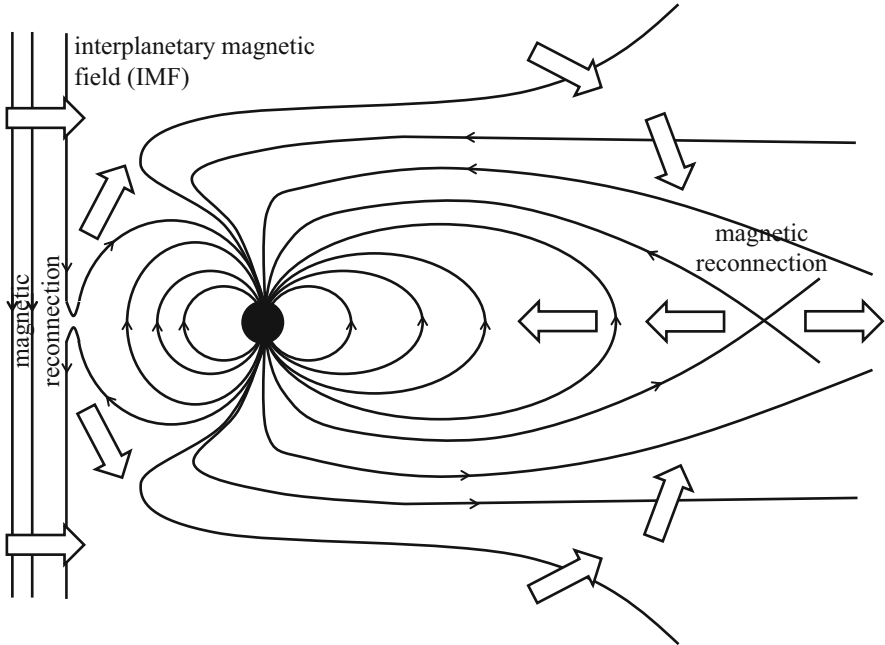
interplanetary magnetic field (IMF)

magnetic reconnection

magnetic reconnection

Fig. 4.3 Schematic of magnetic recombination between day- and nightsides and resulting magnetic field and plasma convection when IMF is southward

earthward plasma and the magnetic field are accelerated in space around the Earth. A part of them is lost into the atmosphere, and the remainder go around the dayside magnetopause. Such a series of plasma convections in the magnetosphere is considered to occur on a timescale of several to 10 h for one revolution.

This magnetic reconnection on the nightside does not necessarily occur continuously; it may occur abruptly after accumulation of the magnetic field flux in the magnetotail. Such an abrupt event is called a magnetospheric substorm, which occurs once or several times a day and lasts from one to several hours. It is also called an auroral substorm, because an aurora in the polar regions shines brightly owing to the injection of high-energy plasma particles into the atmosphere. In contrast, when an IMF turns significantly southward for longer than a few hours, a series of the plasma convections occurs continuously, resulting in a magnetic storm with the intrusion of large amounts of energetic plasma near the Earth. A magnetic storm occurs approximately once a month on average and lasts from one to several days. Magnetic storms occur when systematic plasma and IMF structures are in the solar wind, such as CMEs and co-rotating interaction regions associated with coronal holes, in which the strong southward IMF persists for long periods. Although substorms and magnetic storms have different timescales, both are typical magnetospheric disturbances and intrinsically important for understanding space weather around the Earth.

Fig. 4.4 Schematic of plasma convection in ionosphere at high latitudes (thick solid line). Figure shows view of the Earth from above the North Pole. Outermost circle represents 60° magnetic latitude
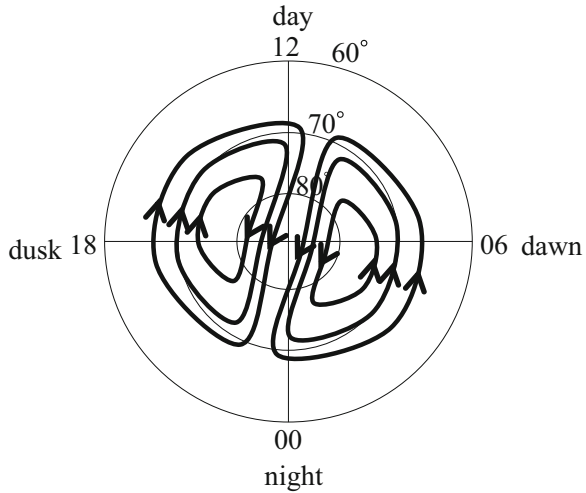
In a substorm, an intense auroral variability and ionospheric currents (auroral electrojet currents) are known to occur in the polar regions. The magnitude of the variability in the horizontal (northward) component of the geomagnetic field caused by the abovementioned ionospheric currents in the auroral zone is indexed by the AU (positive variability), AL (negative variability), and AE (= AU − AL) indices (Davis and Sugiura 1966; WDC-Kyoto et al. 2015a). However, when magnetic storms occur, a ring current, which flows westward in the longitude direction around the Earth, becomes stronger. This current is known to change the geomagnetic field in mid- and low latitudes in a southward direction (decreasing the background northward geomagnetic field). The strength of a magnetic storm is frequently expressed by how negatively the Dst index changes (Sugiura 1964; WDC-Kyoto et al. 2015b). The Dst value indexes the abovementioned mid- and low-latitude variations in the horizontal (northward) component of the geomagnetic field.

Figure 4.4 schematically shows the plasma flow in the magnetosphere illustrated in Fig. 4.3, projected along the magnetic field lines into the ionosphere. The figure looks down on the Earth from above the North Pole, and the magnetic North Pole is at the center. The plasma flow from day to night around the magnetic North Pole corresponds to the plasma that is magnetically reconnected with the IMF on the dayside magnetopause and is swept to the nightside. It can be seen that the plasma injected toward the Earth by the nightside magnetic reconnection flows around the morning and evening sides of the Earth at lower latitudes and subsequently returns to the dayside. Such plasma convections have been observed by high-frequency (HF) radars, which can monitor plasma motions in the ionosphere, and by low-altitude satellites flying in the ionosphere (e.g., Heppner and Maynard 1987; Weimer 1995; Ruohoniemi and Baker 1998).

Figure 4.5 shows the typical motion of plasma sheet particles injected from the magnetotail toward the Earth as a result of its magnetic reconnection. The figure is a
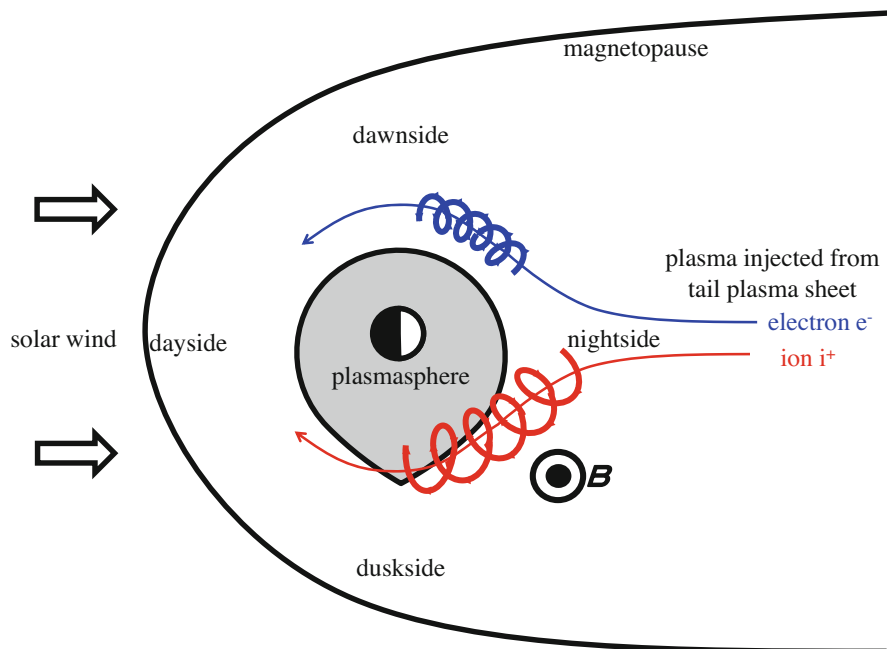
Fig. 4.5 Schematic of plasmasphere and motion of plasma sheet particles injected from magnetotail. The figure shows equatorial cross section of magnetosphere of the Earth viewed from above the North Pole. Schematics of cyclotron motions of ions (red) and electrons (blue) are also shown

schematic of the inner magnetosphere, which is within ten times the Re, in the equatorial cross section viewed from above the North Pole. The electrons and ions constituting the plasma start to drift eastward (morning side) and westward (evening side), respectively, when they approach the Earth. This is because the radius of the cyclotron motion decreases on approaching the Earth and increases on going far from it, as shown by the red and blue rotating lines in the figure. This is due to the earthward gradient of the magnetic field strength and the curvature of the geomagnetic field. Because the rotation directions of the cyclotron motions of the ions and the electrons are opposite, they are separated into westward and eastward directions, respectively. For the theoretical derivation of this magnetic field gradient drift and the curvature drift velocity, please refer to plasma physics textbooks such as by Nicholson (1986). The abovementioned longitudinally drifting high-energy plasma of several keV to several tens of keV spatially overlaps with low-energy (less than several eV) dense plasmas in the plasmasphere and interacts with them to produce various phenomena in the inner magnetosphere. In addition, some of these injected electrons are further accelerated from several hundred keV to several MeV in energy by interaction with electromagnetic waves, forming the radiation belts. The generation and propagation of these electromagnetic waves are influenced by the
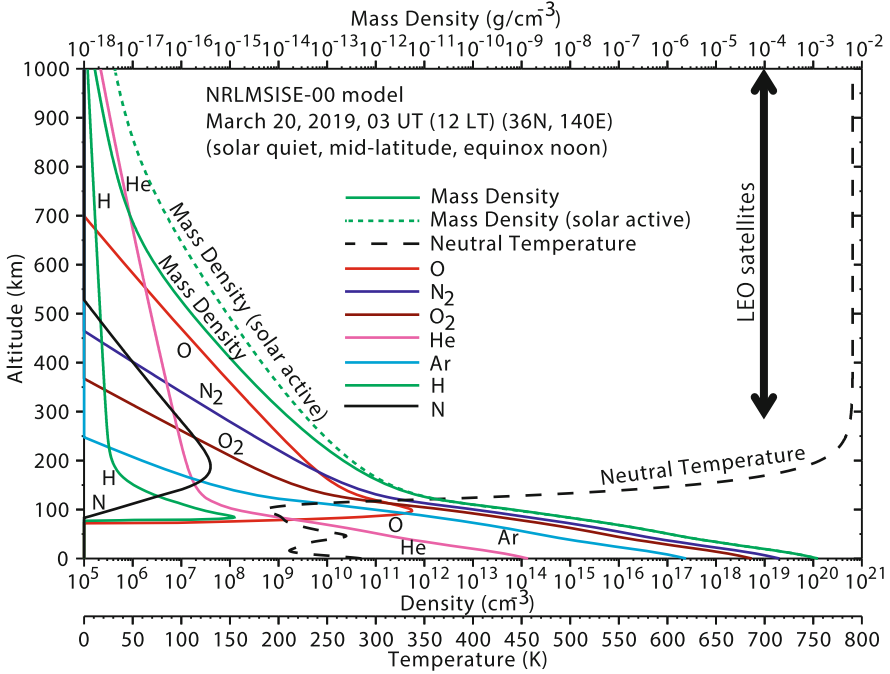
Fig. 4.6 Altitude profiles of neutral atmosphere density and its main composition and temperature at midlatitude (36°N, 140°E) and vernal noon (03 universal time (UT) = 12 LT) during solar activity minimum (March 20, 2019) obtained using from NRLMSISE-00 model. Green dotted line is mass density at same time and location during solar activity maximum (March 20, 2003), as calculated by the Community Coordinated Modeling Center at Goddard Space Flight Center of the National Aeronautics and Space Administration (https://ccmc.gsfc.nasa.gov/modelweb/)

low-energy plasma in the plasmasphere. Thus, the inner magnetosphere is an important region for space weather prediction. This is because the complex interaction of plasma particles with energies of more than six orders of magnitude from eV to MeV with the electromagnetic field and the electromagnetic waves generates the radiation belts, which affect safe and secure space utilization.

Thus far, we have presented various characteristics of the magnetosphere of the Earth, which significantly vary as it interacts with the solar wind. The magnetic field lines of the magnetosphere are concentrated toward the Earth and connected to the atmosphere, as shown in Fig. 4.2. The upper layer of the atmosphere of the Earth is ionized by the solar ultraviolet radiation and forms the ionosphere, which supplies plasma to the magnetosphere, similar to the case of the plasmasphere. Moreover, the ionosphere is electrically connected to the magnetosphere through magnetic field-aligned currents, and acts mainly as a load on the magnetosphere, in terms of an electric circuit.

To understand the structure of the ionosphere, we first show the altitudinal distribution of the atmospheric density and its composition in Fig. 4.6. This figure

shows the atmospheric density at midlatitudes (over Japan) at 12:00 (local time (LT)) on March 20, 2019 (the vernal equinox of the solar activity minimum) obtained using the NRLMSISE-00 model (Picone et al. 2002). Up to an altitude of approximately 100 km, the atmosphere of the Earth consists mainly of nitrogen (N_2) and oxygen (O_2) molecules. From 100 km upward, oxygen molecules are converted to oxygen atoms (O) by photodissociation in sunlight, and gravitational diffusion separation (molecular diffusion) becomes more effective. Thus, oxygen (O), helium (He), and hydrogen (H) atoms are the main components in order of their weights from low to high altitudes. The altitude range in which the atmospheric density becomes 1/e (scale height) is approximately 6–8 km below 120 km, whereas it increases rapidly 30–50 km above 120 km.

The temperature of the atmosphere (the black dashed curve in Fig. 4.6) decreases with distance from the ground (a heat source) up to approximately 10 km of altitude. This region is called the troposphere, in which convection is caused by this negative temperature gradient. Above the tropopause, ozone absorbs the solar ultraviolet radiation and becomes another heat source, temporarily raising the temperature to form the stratosphere and the mesosphere (regions of positive and negative temperature gradients, respectively). Above the mesopause at an altitude of approximately 90 km, the atmosphere is heated, because it is the altitude region where the atmosphere mainly absorbs the ultraviolet radiation from the Sun, and the temperature increases rapidly with the altitude to form the thermosphere. The temperature at the upper end of the thermosphere is approximately 800 K during the solar minimum, whereas it rises to more than 1000 K during the solar maximum.

Most of the LEO satellites and space stations, which are frequently used in space applications, fly in an altitude range of 300–1000 km, as shown by the arrows in Fig. 4.6. This is because it is difficult to maintain a satellite in space for a long period below ~300 km as it can undergo large collisions with the atmosphere (atmospheric drag). Comparing the solid green (solar minimum period; March 20, 2019) and dotted (solar maximum period; March 20, 2003) lines in Fig. 4.6, in the solar maximum period, the mass density of the thermosphere in which a satellite flies increases more than twice than in the solar minimum period. This suggests that the solar activity plays a major role in the lifetime of a satellite.

Figure 4.7 shows the altitudinal distributions of the density of the ionized atmosphere and its composition and electron and ion temperatures. It presents the electron density in the ionosphere at 12:00 noon (03 UT) at midlatitudes (over Japan) on March 20, 2019 (the vernal equinox of the solar activity minimum) using the IRI-2012 model (Bilitza et al. 2014). The temperature of the neutral atmosphere shown at the same time is based on the CIRA-86 model (Fleming et al. 1990). The difference between the terms "electron density" and "plasma density" is that in a plasma consisting of monovalent ions and electrons, the electron density (density of negative charges) and the ion density (density of positive charges) are typically equal. Therefore, the two terms are frequently used synonymously. Because the plasma density of the ionosphere has historically been measured as the electron density by the reflection of radio waves contributed by electrons, the plasma density is generally expressed as the electron density.
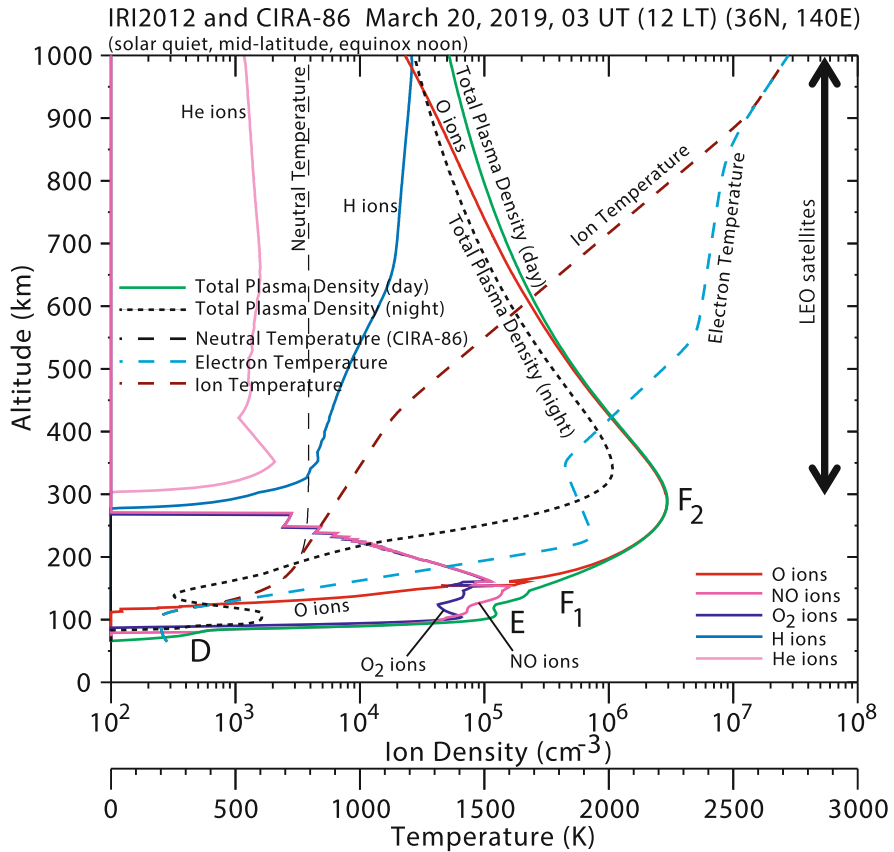
Fig. 4.7 Altitude profiles of ionospheric electron density, its representative composition, and ion and electron temperature from the IRI-2012 model at midlatitudes during solar minimum, spring equinox daytime, as calculated by the Community Coordinated Modeling Center at Goddard Space Flight Center of National Aeronautics and Space Administration (https://ccmc.gsfc.nasa.gov/modelweb/)

The daytime ionosphere has local peaks and bulges in the D, E, F_1, and F_2 layers from the bottom. These can be attributed to the wavelength distribution of the corresponding solar ultraviolet radiation, compositional distribution of the atmosphere, and recombination reactions between the neutral and ionized atmospheres. The E layer is dominated by NO^+ and O_2^+, whereas the F layer is dominated by O^+. H^+ becomes the dominant component at heights above 1000 km. The D layer (D region) is dominated by complex molecular ions called hydrated and cluster ions, which are formed from NO^+ and O_2^+ by various chemical reactions.

The electron density at the peak height of the F layer, where the density of the ionosphere is the highest, is approximately 10^6 cm^{-3}. The density of the neutral atmosphere at the same altitude of ~300 km is approximately 10^9 cm^{-3}, i.e., only

1 out of 1000 atoms and molecules in the atmosphere is ionized at the highest level. Therefore, the dynamical variability in the ionospheric plasma is significantly influenced by the winds of the neutral atmosphere.

The ionospheric electron density at 00:00 (15 UT) on the same day and at the same location is also shown by a dotted line in Fig. 4.7. Because there is no ionization source at night, the recombination due to the collision between the ionospheric plasma and the neutral atmosphere gradually progresses from the lower part. Moreover, the peak height of the ionospheric F layer increases and the overall electron density drops to less than half. At night, the E layer almost disappears owing to the recombination; however, as described in Chap. 7, metal ion accumulation is caused by the vertical wind shear of the neutral atmosphere, and a layer called the sporadic E layer abruptly emerges.

LEO satellites and space stations fly above the peak altitude of the ionospheric F layer for the most part because of their altitudes above 300 km. Therefore, the communication with the ground is strongly affected by the plasma in the ionosphere.

The electron density in the ionosphere is generally high near the equator, where the solar ultraviolet radiation is the strongest, and decreases to less than half as it approaches both poles. The latitudes at which the density reaches its maximum are approximately 5–15° north and south of the magnetic equator and are called the equatorial ionization anomaly. The equatorial ionization anomaly occurs because the plasma generated at the magnetic equator is lifted by the eastward electric field during the daytime and redistributed along the magnetic field lines to high latitudes by the gravitational force of the Earth. Thus, the density of the ionosphere is at its maximum at the equatorial ionization anomaly, where the impact on positioning and communication also becomes maximum.

Similar to the magnetospheric plasma, the ionospheric plasma dynamically varies. The ionospheric electron density is broadly determined by the balance between the production by the solar ultraviolet radiation, quenching by recombination with the neutral atmosphere, and diffusion along the geomagnetic field lines. In particular, the ionospheric plasma in the F layer is subject to an $\mathbf{E} \times \mathbf{B}$ drift due to the east–west electric field and the northward magnetic field and flows with velocity $\boldsymbol{v} = (\boldsymbol{E} \times \boldsymbol{B})/B^2$ in the direction of the product of the electric field, $\boldsymbol{E}$, and the magnetic field, $\boldsymbol{B}$. The eastward electric field increases the altitude of the ionosphere, whereas the westward electric field decreases it. Both electric fields may be transmitted to the ionosphere by solar wind–magnetosphere interactions, magnetospheric storms, and substorms.

The plasma in the ionospheric F layer is also shifted up and down along the magnetic field lines by the meridional winds in the neutral atmosphere. Because the plasma in the ionosphere cannot move across a magnetic field line owing to its cyclotron motion, the poleward winds push the plasma down along the geomagnetic field lines, whereas the equatorward winds push it up at midlatitudes. The winds in the neutral atmosphere (thermosphere) are dominated by thermospheric tides, which have a 1-day cycle, and they blow from the warmed dayside atmosphere to the cooler nightside atmosphere. Therefore, the daytime ionosphere tends to be pushed down by the poleward winds, whereas the nighttime ionosphere tends to be lifted by the

equatorward winds. In addition, atmospheric waves propagating from the lower atmosphere (such as atmospheric gravity waves, harmonics of atmospheric tides, and planetary waves) and heating of the upper atmosphere at high latitudes due to magnetic storms also produce neutral wind variations in the thermosphere. When the ionosphere is pushed down by the electric field and neutral winds, the density of the ionospheric plasma decreases as it recombines with the higher-density neutral atmosphere at lower altitudes.

In addition to these external ionospheric disturbances, the ionospheric plasma itself causes fluid-like plasma instabilities, as described in Chap. 7. Most of them are Rayleigh–Taylor-type instabilities, such as plasma bubbles at equatorial latitudes and medium-scale traveling ionospheric disturbances at midlatitudes, both increased by an $\mathbf{E} \times \mathbf{B}$ drift due to the polarized electric field. A gradient drift instability, which is caused by the density gradient of the ionospheric plasma and the current flowing orthogonally to it, is also broadly a Rayleigh–Taylor-type plasma instability. These ionospheric plasma instabilities are important for understanding space weather, because they produce subkilometer-scale plasma structures in the ionosphere, which cause interferences in the radio waves used for satellite-to-ground communication and satellite positioning.

4.2 Measurement of Magnetosphere and Ionosphere of the Earth

The structures of and variations in the magnetosphere and ionosphere of the Earth described thus far have been clarified by various measurements using instruments on board satellites and remote sensing instruments on the ground. Thus, the knowledge of the magnetosphere and the ionosphere is strongly connected with the measurement techniques, and understanding of these measurement techniques is indispensable for the understanding of the magnetosphere and the ionosphere. In this section, we briefly introduce the representative measurement techniques for the terrestrial magnetosphere and ionosphere.

The plasma and the electromagnetic field in the magnetosphere of the Earth, except the electromagnetic waves propagating to the ground, are difficult to observe from the ground by remote sensing. Thus, they have been measured by direct (in situ) observations using satellites. Fig. 4.8 shows the instruments and their energy and frequency ranges used to measure the plasma and the electromagnetic field using the Exploration of Energization and Radiation in Geospace (also called Arase) satellite of Japan, which observes the magnetosphere around the Earth (Miyoshi et al. 2018). Typical examples of the data observed by these instruments are presented in Fig. 4.9. The Arase satellite is a satellite that observes the inner magnetosphere with an apogee altitude of ~32,000 km, a perigee altitude of ~440 km, and an orbital period of ~10 h. This satellite is a typical magnetospheric satellite that carries major plasma and electromagnetic field instruments besides
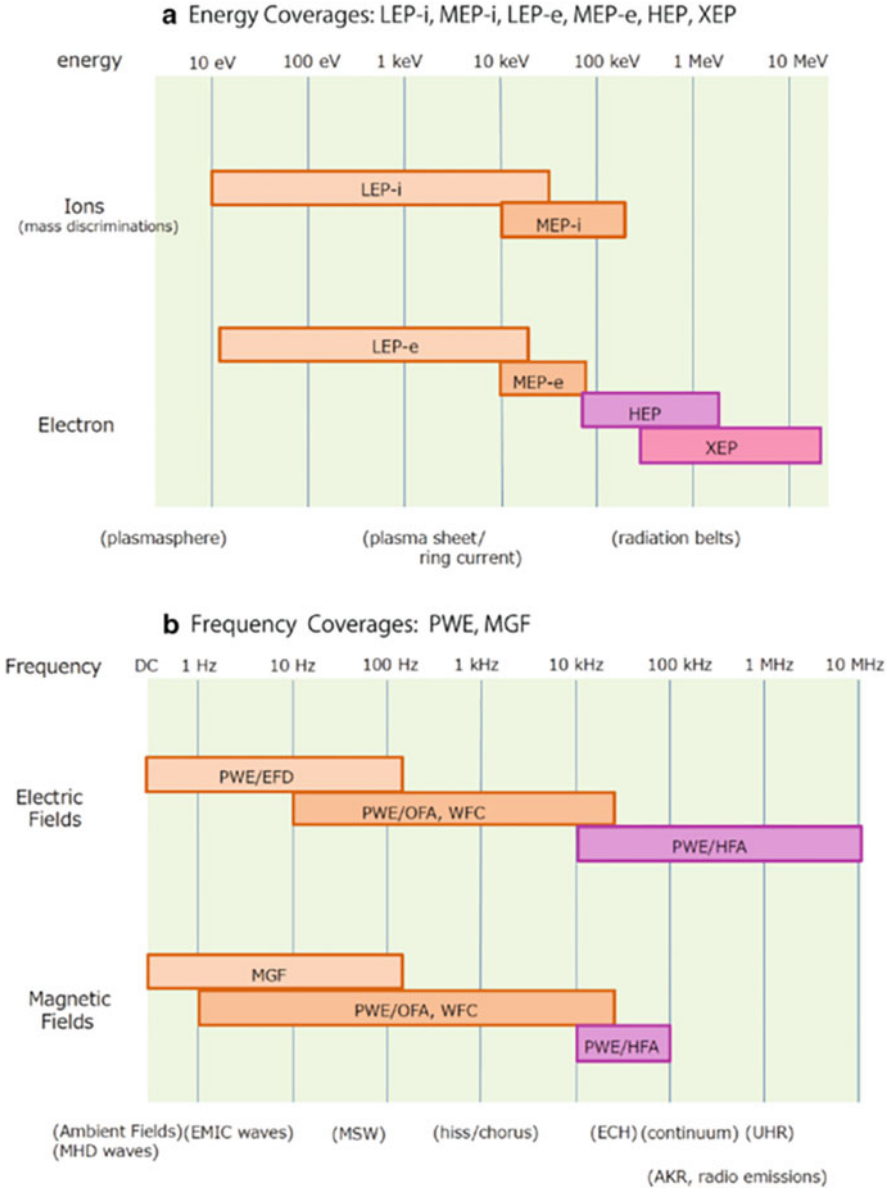
Fig. 4.8 (**a**) Measured energy ranges of particle instruments and (**b**) measured frequency ranges of electromagnetic field instruments on board Arase satellite (Miyoshi et al. 2018)

optical instruments. Other such satellites are the Time History of Events and Macroscale Interactions during Substorms and Radiation Belt Storm Probes satellites of the United States and the Geotail satellite of Japan. Figure 4.8a shows six instruments that measure ions (i) and electrons (e) and their measured energy ranges.
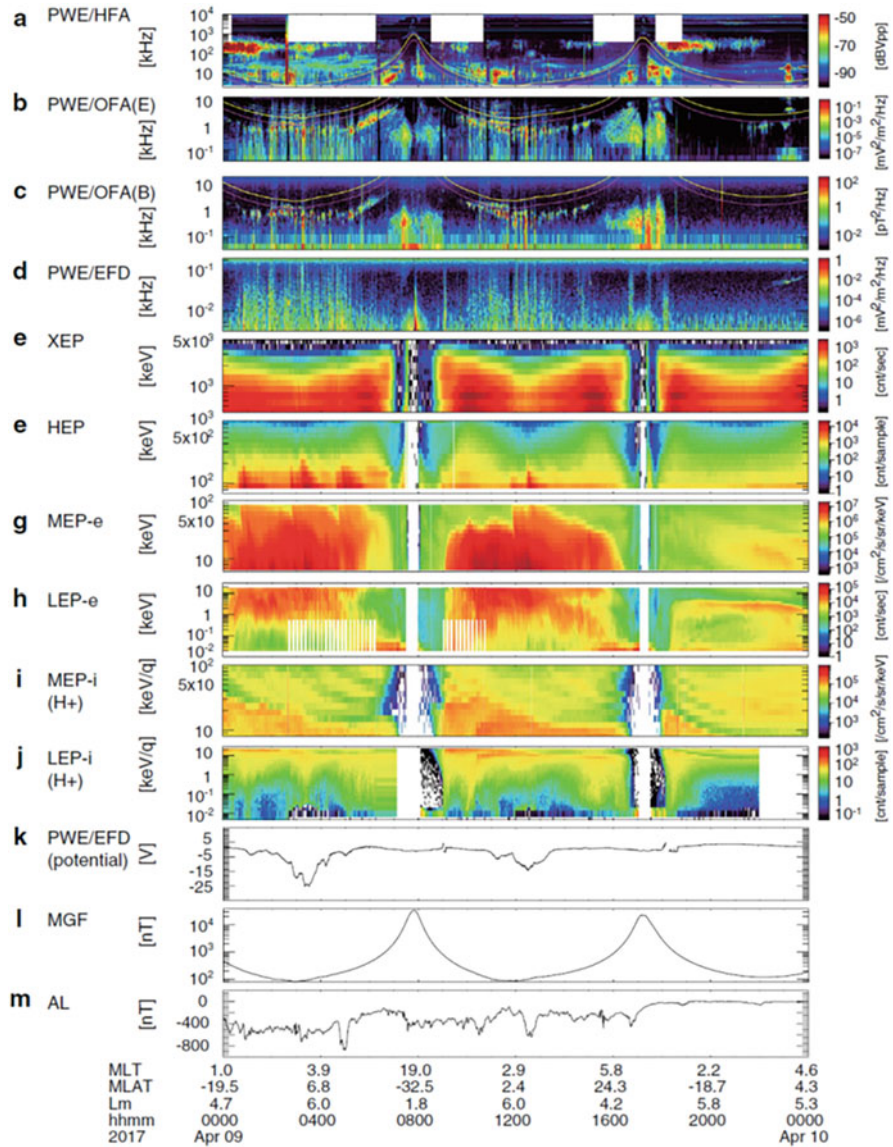
Fig. 4.9 (**a–d**) Frequency spectrum of electromagnetic waves, (**e–j**) energy–time spectrum of plasma particles, (**k**) satellite potential, (**l**) magnetic field strength, and (**m**) AL index observed by Arase satellite (Miyoshi et al. 2018)

Low-energy particle experiments, ion mass analyzer (LEP-i); low-energy particle experiments, electron analyzer (LEP-e); medium-energy particle experiments, ion mass analyzer (MEP-i); and medium-energy particle experiments, electron analyzer (MEP-e), at the low-energy side use the principle of an electrostatic analyzer, which

is a device that applies a constant electric field between two parallel plates and counts only the charged particles that pass between them. MEP-i and MEP-e also use a new technology called an avalanche photodiode (Kasahara et al. 2018; Yokota et al. 2017). Using an electrostatic analyzer, the number of particles at an energy is measured by changing the strength of the electric field between two parallel plates stepwise. However, to avoid discharge accidents, the strength of the electric field between the two plates is typically limited to be less than a few kilovolts. Thus, the energy of the particles that can be measured has an upper limit of tens to hundreds of keV. For particles with higher energies, a solid-state detector is used to directly count them and simultaneously measure their energy from the magnitude of the output pulse. Because the measurement principle and energy range of the different instruments vary, simultaneous measurement of the energy distribution function of plasma particles over a wide energy range from 20 eV to more than 10 MeV is realized by installing multiple instruments.

Panels (e)–(j) in Fig. 4.9 show the particle flux measured by these plasma particle detectors in color. The vertical axis is the energy, and the horizontal axis is the time, with the satellite position moving from the ionosphere near the Earth (0800 universal time (UT) and 1800 UT) to the magnetosphere with an orbital period of approximately 10 h. Note that the units of the different colors are slightly different. In MEP-i and MEP-e, whose instruments are calibrated, the color unit is [/cm^2/s/sr/keV], which indicates the number particles entered per unit area [cm^2], unit time [s], unit solid angle [sr], and unit energy [keV]. By calibrating the sensitivity of each particle detector and adjusting it to the same units, a uniform particle distribution function over a wide energy range can be obtained. However, the calibration of the absolute sensitivity of particle detectors may include systematic errors due to various factors, and their fields of view and energy resolutions are different. Thus, comparing and matching the distribution functions obtained by different instruments are difficult tasks, which could become research topics.

Figure 4.8b shows six instruments that measure the electric and magnetic fields and their ranges of measurement frequencies. The magnetic field is measured over a wide range of frequencies using fluxgate magnetometers (MGFs), which measure low frequencies from DC to 128 Hz, and search coil magnetometers (plasma wave experiment (PWE)/onboard frequency analyzer (OFA), PWE/high-frequency analyzer (HFA)), which measure high frequencies. These magnetometers are mounted on the top of a 5-meter-long mast to avoid the magnetic field noise generated by the satellite body. The electric field is measured by four (two pairs) 15-meter-long wire antennas stretched out in the satellite spin plane. The electric field variations in space obtained from these antennas are divided into three frequency bands by three types of receivers: PWE/EFD, PWE/OFA-WFC, and PWE/HFA. Although the electric field perpendicular to the spin surface cannot be measured, the x, y, and z components of the magnetic field can be obtained. By assuming that the electric field along a magnetic field line is zero, we can obtain the third component of the electric field from the equation, $\boldsymbol{E} \cdot \boldsymbol{B} = 0$.

Figure 4.9a, b, and d shows the electric field variations in the abovementioned three frequency bands, and Fig. 4.9c and i presents the wave and DC components of

the magnetic field measured by a search coil magnetometer and a fluxgate magnetometer, respectively. The satellite potential shown in Fig. 4.9k is not the potential difference between the two ends of a single-wire antenna but the potential at the root of the antenna, which represents the potential of the satellite relative to that of the surrounding plasma. This value varies with the density and temperature of the plasma around the satellite, and the plasma density can be estimated from this value.

As presented in Fig. 4.8a, the particle detectors cannot measure the distribution function of the plasma below 10–20 eV. This is because if the particle energy is extremely low, it is affected by the potential of the satellite body, and accurate measurement is impossible. Such low-energy plasmas, as represented by the plasmasphere, account for most of the plasma density in space and are important phenomena that have significant effects on the excitation and propagation of electromagnetic waves. The background plasma density can be accurately estimated from the frequency, f_{UHR}, of the upper hybrid resonance (UHR), which is characteristically strong at a single frequency of 10–1000 kHz. The f_{UHR} is a function of the plasma frequency, f_p, and the cyclotron frequency, f_c, as $f_{\mathrm{UHR}}^2 = f_p^2 + f_c^2$. The value of f_c is obtained from the magnetic field strength measured by a fluxgate magnetometer. Therefore, we can estimate the plasma frequency, f_p, and, thus, the ambient plasma density, from the f_{UHR} measured from a high-frequency wave spectrum at 10–1000 kHz.

As described above, satellites have performed numerous direct in situ observations of the magnetosphere of the Earth, providing a schematic of the dynamic variations in the magnetosphere, which is presented in Sect. 2.1.1. In addition, to visualize the global picture of the magnetosphere, resonant scattering of sunlight by plasmasphere ions and high-energy neutral particles from ring current ions moving away from the magnetic field lines have been received by satellites in combination with wide-area auroral images from high altitudes, such as those by the IMAGE satellite (Mitchell et al. 2000; Mende et al. 2000; Goldstein and Sandel 2005). In the future, there are plans to image the magnetosphere using electromagnetic waves that propagate straight, irrespective of the ambient magnetic field and the plasma density, such as X-rays (Sibeck et al. 2018).

In the ionosphere, which is closer to the Earth than the magnetosphere, direct measurements from LEO satellites using plasma particles and electromagnetic field instruments have been conducted, similarly to those in the magnetosphere. Remote sensing measurements from the ground have also been conducted for a long time. Figure 4.10 summarizes the measurement altitude ranges and measurement parameters of major ground-based remote sensing instruments. Broadly, from left to right, these are radars, which emit radio waves from the ground and measure the reflected waves from the ionosphere; radio receivers, which receive radio waves emitted by satellites at altitudes higher than the ionosphere on the ground; radio receivers which measure natural radio waves in the very-low-frequency (VLF) band, low-frequency (LF) band, and millimeter-wave band and magnetic field fluctuations of natural origin; spectrometers and interferometers, which receive atmospheric light emitted
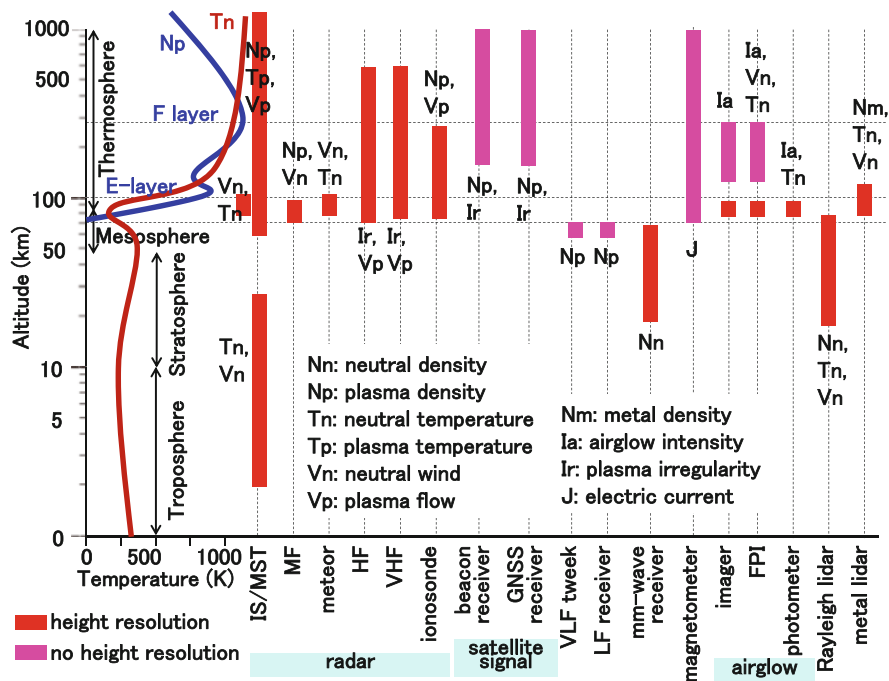
Fig. 4.10 Schematic of ground-based instruments and measurement altitudes in upper atmosphere and ionosphere (Oberheide et al. 2015)

in the ionosphere; and lidars, which emit laser beams and measure the reflected lights. Typical instruments are briefly introduced below.

1. Ionosonde: It is a radar that has long been used to observe the ionosphere. It emits radio waves in a frequency range from 2 to 20 MHz from the ground and measures the reflection from the ionosphere. By measuring the time difference between the emission and the reflection while changing the frequency, the altitude of each electron density in the lower ionosphere (e.g., h'E and h'F) and the peak electron density in the ionosphere (e.g., foE and foF) can be determined. This instrument has been operated in many countries since the International Earth Observation Year in 1957 and has significantly contributed to the development of the ionospheric standard model.

2. Incoherent scattering radar: It is a radar that emits powerful radio waves from the ground and captures the radio waves that are reflected very weakly by the random thermal motion of the electrons in the ionosphere. It can measure the electron density distribution and the velocity of the plasma motion in the ionosphere at all altitudes, from lower to upper levels. It requires a large antenna with a large aperture and a high output power of several megawatts or more, making it a large-scale facility of several billion yen in value. Therefore, there are only less than ten such devices in the world, such as the European Incoherent Scatter (EISCAT)

radar in Scandinavia, Jicamarca radar in Peru, Arecibo radar in Puerto Rico, and middle and upper atmosphere (MU) radar in Japan.

3. Coherent scattering radar: When there are repeating thick and thin electron density structures in the ionosphere and the spatial scale of the repetition is the same as the half-wavelength of a radar radio wave, the radio wave can be scattered efficiently. Because this scattering is much stronger than the incoherent scattering described above, the ionosphere can be observed with a relatively inexpensive radar with an output power of approximately several kilowatts. However, observation is impossible unless electron density structures are present in the ionosphere. Therefore, radar radio waves do not always return, and the measurement direction and time are limited. The Super Dual Auroral Radar Network (SuperDARN) radars, which are commonly used in the polar regions, and VHF radars, which are employed in the equatorial regions, are such coherent scatter radars with interferometric capability to have two-dimensional field of views.

4. GNSS receiver: Radio signals from the Global Navigation Satellite System (GNSS) satellites, which are commonly used for positioning, present a delay proportional to the ionospheric electron density when they pass through the ionosphere. The total electron content (TEC) of the ionosphere, integrated in the direction of altitude, can be obtained by measuring this delay. In recent years, to measure crustal movement, more than 1000 GNSS receivers have been installed over Japan by its Geospatial Information Authority. This multipoint network enables two-dimensional imaging observations of the TEC in the ionosphere. The TEC distribution in the ionosphere along the orbit of a satellite can also be measured in approximately 10 min by receiving radio waves from LEO satellites, which move with quite a high speed (~8 km/s) when viewed from the ground, instead of the GNSS satellites.

5. VLF tweeks and LF radio receivers: LF-band standard radio waves have been used to set the times of radio clocks. VLF-band tweek radio waves are emitted by lightning discharges. These LF/VLF waves spread across the Earth while propagating through the duct between the ground and the ionospheric D layer. By receiving these radio waves, altitude changes in the lower ionospheric D layer, which are difficult to measure with radars such as ionosondes, can be monitored from the ground.

6. Millimeter-wave receiver: Atmospheric minor constituents such as ozone and nitrogen oxides in the upper atmosphere emit radio waves in the millimeter-wave band. By receiving these radio waves, the amounts and fluctuations of these minor constituents can be measured from the ground.

7. Magnetometer: Magnetometers measure the geomagnetic variations that are mainly caused by the currents in the magnetosphere and the ionosphere. In particular, the current flowing in the ionosphere contributes the most to the magnetic field variations on the ground. By installing magnetometers at multiple points on the ground, a two-dimensional distribution of the ionospheric currents and its time evolution can be observed. Combining this distribution with magnetic field fluctuations observed by satellites, there are also efforts to obtain a

three-dimensional structure of the ionospheric, magnetospheric, and field-aligned electric currents. The measurement of geomagnetic variations is essential as the input information for the measurement and modeling of GICs, which are major phenomena in space weather. Geomagnetic variations also present characteristic oscillations called geomagnetic pulsations, which have periods of approximately 0.2 s–10 min. From these geomagnetic pulsations, it is possible to diagnose phenomena in the magnetosphere and ionosphere of the Earth, such as predicting the occurrence of substorms using Pi2 geomagnetic pulsations and measuring the plasmasphere density through field-line resonance frequencies.

8. Airglow imager and Fabry–Perot interferometer: Because nocturnal airglows and auroras originate at altitudes of 80–300 km with a constant emission layer at each wavelength, their imaging observation is possible from the ground. Fabry–Perot interferometers have been used to measure the neutral and plasma velocities in the upper atmosphere by the Doppler shift of the emission lines of auroras and airglows.

9. Lidar: An optical laser beam is launched into the sky to measure scattered laser lights, which can be used to measure the density, temperature, and wind speed of the scattering atmosphere. In particular, a metal lidar, which measures the resonant scattering of metal ions such as sodium, iron, and calcium at altitudes of 80–110 km, is an important instrument that can measure the atmosphere at altitudes of 100 km or higher, which is difficult by other instruments.

As described above, the ionosphere and the upper atmosphere have been observed from the ground by various instruments as well as by satellites. Although satellites can directly observe geophysical quantities in situ, because they move at high speeds, they cannot determine changes over time at a fixed point. In contrast, remote sensing from the ground can measure for a long time at a fixed point; however, the physical quantity that can be measured varies depending on the instrument, and there are several measurement limitations. To understand the changes in the ionosphere and the upper atmosphere, it is very important to combine the advantages of various instruments, instead of being limited to measurements of one type of instrument.

References

Bilitza, D., Altadill, D., Zhang, Y., Mertens, C., Truhlik, V., Richards, P., McKinnell, L.-A., Reinisch, B.: The International Reference Ionosphere 2012 - A model of international collaboration. J. Space Weather Space Clim. **4**(A07), 1–12 (2014). https://doi.org/10.1051/swsc/2014004

Davis, N., Sugiura, M.: Auroral electrojet activity index AE and its universal time variations. J. Geophys. Res. **71**(3), 785–801 (1966). https://doi.org/10.1029/JZ071i003p00785

Dungey, J.W.: The structure of the exosphere or adventure in velocity space. In Geophysics, p. 505. Gordon and Breach Science Publishers, London (1962)

Fleming, E.L., Chandra, S., Barnett, J.J., Corney, M.: Zonal mean temperature, pressure, zonal wind, and geopotential height as functions of latitude, COSPAR International Reference

Atmosphere: 1986, Part II: middle atmosphere models. Adv. Space Res. **10**(12), 11–59 (1990). https://doi.org/10.1016/0273-1177(90)90386-E

Goldstein, J., Sandel, B.R.: The global pattern of evolution of plasmaspheric drainage plumes. In: Burch, J.L., Schulz, M., Spence, H. (eds.) Inner Magnetosphere Interactions: New Perspectives from Imaging, p. 1. American Geophysical Union, Washington, DC (2005). https://doi.org/10.1029/2004BK000104

Heppner, J.P., Maynard, N.C.: Empirical high-latitude electric field models. J. Geophys. Res. **92**(A5), 4467–4489 (1987). https://doi.org/10.1029/JA092iA05p04467

Kasahara, S., Yokota, S., Mitani, T., Asamura, K., Hirahara, M., Shibano, Y., Takashima, T.: Medium-energy particle experiments - electron analyser (MEP-e) for the exploration of energization and radiation in Geospace (ERG) mission. Earth Planets Space. **70**(1), 1–6 (2018). https://doi.org/10.1186/s40623-018-0847-z

Mende, S.B., et al.: Far ultraviolet imaging from the IMAGE spacecraft. 2, wideband FUV imaging. Space Sci. Rev. **91**, 271–285 (2000)

Mitchell, D.G., et al.: High energy neutral atom (HENA) imager for the image mission. Space Sci. Rev. **91**, 67–112 (2000)

Miyoshi, Y., et al.: Geospace exploration project ERG. Earth Planets Space. **70**, 101 (2018). https://doi.org/10.1186/s40623-018-0862-0

Nicholson, D.R.: Introduction to plasma theory, Wiley (1986), 日本語訳:プラズマ物理の基礎、小笠原正忠・加藤鞴一共訳、丸善(1986)

Nishida, A.: Formation of plasmapause, or magnetospheric plasma knee, by the combined action of magnetospheric convection and plasma escape from the tail. J. Geophys. Res. **71**(23), 5669–5679 (1966). https://doi.org/10.1029/JZ071i023p05669

Oberheide, J., Shiokawa, K., Gurubaran, S., Ward, W.E., Fujiwara, H., Kosch, M.J., Makela, J.J., Takahashi, H.: The geospace response to variable inputs from the lower atmosphere: a review of the progress made by task group 4 of CAWSES-II. Progr. Earth Planet. Sci. **2**, 2 (2015). https://doi.org/10.1186/s40645-014-0031-4

Picone, J.M., Hedin, A.E., Drob, D.P., Aikin, A.C.: NRLMSISE-00 empirical model of the atmosphere: statistical comparisons and scientific issues. J. Geophys. Res. **107**(A12), 1468 (2002). https://doi.org/10.1029/2002JA009430

Ruohoniemi, J.M., Baker, K.B.: Large-scale imaging of high-latitude convection with super dual auroral radar network HF radar observations. J. Geophys. Res. **103**(9), 20797–20811 (1998). https://doi.org/10.1029/98JA01288

Sibeck, D., et al.: Imaging plasma density structures in the soft X-rays generated by solar wind charge exchange with neutrals. Space Sci. Rev. **214**(4), 1–24 (2018). https://doi.org/10.1007/s11214-018-0504-7

Sugiura, M.: Hourly values of equatorial Dst for the IGY. In Annals of the International Geophysical Year, vol. 35, pp. 7–45. Pergamon Press, Oxford (1964)

Weimer, D.R.: Models of high-latitude electric potentials derived with a least error fit of spherical harmonic coefficients. J. Geophys. Res. **100**, 19595–19607 (1995)

World Data Center for Geomagnetism, Kyoto, M. Nose, T. Iyemori, M. Sugiura, T. Kamei, Geomagnetic AE index, https://doi.org/10.17593/15031-54800 (2015a)

World Data Center for Geomagnetism, Kyoto, M. Nose, T. Iyemori, M. Sugiura, T. Kamei, Geomagnetic Dst index, https://doi.org/10.17593/14515-74000 (2015b)

Yokota, S., Kasahara, S., Mitani, T., Asamura, K., Hirahara, M., Takashima, T., Yamamoto, K., Shibano, Y.: Medium-energy particle experiments--ion mass analyzer (MEP-i) onboard ERG (Arase). Earth Planets Space. **69**, 172 (2017). https://doi.org/10.1186/s40623-017-0754-8